

In vivo high-resolution 3D photoacoustic imaging of superficial vascular anatomy

E Z Zhang¹, J G Laufer¹, R B Pedley² and P C Beard¹

¹ Department of Medical Physics and Bioengineering, University College London, Gower Street, London, WC1E 6BT, UK

² UCL Cancer Institute, Paul O’Gorman Building, University College London, 72 Huntley St, London WC1E 6BT, UK


Received 21 October 2008, in final form 22 December 2008

Published 23 January 2009

Online at stacks.iop.org/PMB/54/1035

Abstract

The application of a photoacoustic imaging instrument based upon a Fabry–Perot polymer film ultrasound sensor to imaging the superficial vasculature is described. This approach provides a backward mode-sensing configuration that has the potential to overcome the limitations of current piezoelectric based detection systems used in superficial photoacoustic imaging. The system has been evaluated by obtaining non-invasive images of the vasculature in human and mouse skin as well as mouse models of human colorectal tumours. These studies showed that the system can provide high-resolution 3D images of vascular structures to depths of up to 5 mm. It is considered that this type of instrument may find a role in the clinical assessment of conditions characterized by changes in the vasculature such as skin tumours and superficial soft tissue damage due to burns, wounds or ulceration. It may also find application in the characterization of small animal cancer models where it is important to follow the tumour vasculature over time in order to study its development and/or response to therapy.

 This article features online multimedia enhancements

(Some figures in this article are in colour only in the electronic version)

1. Introduction

The non-invasive characterization of the structure, oxygenation and flow status of the vasculature within a few mm of the surface of the skin is required for a broad range of clinical and basic research studies. Clinical applications include the assessment of skin tumours, abnormalities of the microcirculation in patients with lower limb venous disease and diabetes, soft tissue damage such as burns and ulceration and other conditions characterized by changes in tissue perfusion and oxygenation. There is also a need to characterize small animal models

of these and other conditions for the pre-clinical development of new therapies. For example, the ability to monitor non-invasively the development of the vasculature in subcutaneously implanted tumours in mice would be of benefit to the study of antivasular drugs and other treatments.

Optical techniques offer the prospect, at least in principle, of characterizing superficial vascular anatomy and function. The strong preferential optical absorption of blood offers high contrast, the spectral differences between oxy- and deoxyhaemoglobin allows blood oxygen saturation to be determined and Doppler techniques can be used to measure flow. In addition, the relative transparency of tissue to near-infrared (NIR) light in the range 600 nm–900 nm enables penetration depths of many mm to be achieved. However, a major limitation is that spatial resolution degrades rapidly for depths beyond approximately 1 mm due to overwhelming optical scattering in most tissues. Ultrasound imaging on the other hand can readily provide spatial resolutions on a scale of tens to hundreds of microns for sub-cm depths. This is a consequence of the much lower scattering that acoustic waves undergo in soft tissues compared to photons. However, the low echogenicity of microvessels makes it difficult to visualize the microvasculature without the use of contrast agents. Furthermore, although ultrasound can be used to determine blood flow by exploiting the Doppler effect, it cannot measure blood oxygenation.

Photoacoustic imaging is a relatively new hybrid imaging modality that combines the physics of optical and ultrasound imaging (Xu and Wang 2006). In doing so, it provides both the high contrast and spectroscopic based specificity of optical techniques and the high spatial resolution of ultrasound. The technique involves delivering nanosecond pulses of NIR or visible laser light to the surface of the skin. Absorption of the laser energy results in rapid thermoelastic expansion and the emission of broadband (typically tens of MHz) pulses of ultrasound. The latter propagate to the surface where they are detected at different spatial points using either an array of ultrasound receivers or a single mechanically scanned detector. By measuring the times-of-arrival of the ultrasound pulses at the surface and knowing the speed of sound in tissue, an image of the absorbed optical energy distribution can be reconstructed. Spatial resolution is defined by the physics of ultrasound propagation and is limited by the frequency-dependent attenuating characteristics of soft tissue. Image contrast on the other hand is based largely on optical absorption, which means that the technique is particularly well suited to imaging blood vessels due to the strong optical absorption of haemoglobin. This has now been demonstrated by a number of studies in which 3D images of the vasculature within a few mm of the skin surface have been obtained with a spatial resolution of the order of several tens of microns (Lao *et al* 2008, Siphanto *et al* 2004, Zhang *et al* 2006a, 2006b). Other studies have shown that changes in tissue perfusion characteristic of skin tumours (Oh *et al* 2006), dermal vascular lesions (Viator *et al* 2002) and soft tissue damage such as burns (Zhang *et al* 2006c) can be observed using photoacoustic methods. As well as imaging vascular anatomy, functional information in the form of blood oxygenation and flow can be obtained: the former by acquiring images at multiple wavelengths and exploiting the spectral differences between oxy- and deoxyhaemoglobin (Laufer *et al* 2007, Zhang *et al* 2006a), the latter by extracting the acoustic Doppler shift encoded on to photoacoustic waves emitted by moving red blood cells (Beard 2001, Fang *et al* 2007).

Despite the evident success of photoacoustic imaging for characterizing superficial vascular structures, there are several challenges associated with its practical implementation particularly when using piezoelectric receivers to detect the photoacoustic signals. One of these challenges relates to the delivery of the excitation laser light. Ideally, an optically transparent detector array that can be placed on the skin surface and the excitation laser pulses transmitted through it and into the underlying tissue is required to provide the so-called

backward mode detection configuration. This presents obvious difficulties when using piezoelectric transducers, as the majority are opaque—a notable exception being that described in Niederhauser *et al* (2005). Another challenge is that most image reconstruction algorithms require the detector element size to be small compared to the acoustic wavelength. For superficial imaging applications, where the acoustic propagation distances are of the order of a few mm, the signal is only weakly bandlimited by frequency-dependent acoustic attenuation. This results in very broadband signals (tens of MHz) with wavelengths as small as a few tens of microns. Achieving adequate detection sensitivity with element sizes on this scale then becomes problematic due to the inverse relationship between the active area of a piezoelectric receiver and its sensitivity. The so-called photoacoustic microscopy approach (Wang 2008), which employs a single mechanically scanned focused transducer to map the photoacoustic signals, can overcome these limitations to some extent. With this method, backward mode operation is achieved by locating the transducer at the centre of a conical excitation beam that is focused on the tissue surface. Although high quality images of the vasculature have been obtained with this approach (Zhang *et al* 2006a), the highest lateral spatial resolution is achieved only at a limited range of depths, those that coincide with the non-divergent region of the transducer focus. It also remains to be seen whether this sequential scanning approach can be parallelized in order to overcome the limited acquisition speed associated with mechanical scanning.

In this paper, we describe the use of an alternative detection system for imaging the superficial vasculature that can address these limitations. In this approach, an optical ultrasound sensor based upon a Fabry–Perot polymer film interferometer is used to detect the acoustic signals. Since the sensor head is transparent, backward mode operation can readily be achieved thus avoiding the difficulties of delivering the excitation light encountered when using piezoelectric receivers. In addition, the optical nature of the transduction mechanism enables acoustically small element sizes at MHz frequencies to be obtained with much higher sensitivity than broadband piezoelectric receivers can provide. Furthermore because a tomographic image reconstruction approach is employed, the concept does not suffer from the depth-limited spatial resolution limitations that occur when using a fixed focus transducer and the sensor read-out scheme can readily be parallelized using an optical detector array to achieve high frame rates.

The operating principles of the system and its application to imaging phantoms (Zhang *et al* 2008) and the mouse brain (Zhang *et al* 2007) have been described previously. In this paper, we demonstrate its ability to provide high-resolution 3D images of the vasculature in the skin and subcutaneous tumours grown in mice. Section 2 provides an overview of the imaging system and its performance whilst section 3 presents the images obtained in tissue.

2. Photoacoustic imaging system

2.1. Principles of operation

A full description of the imaging system is provided in Zhang *et al* (2008) so only a brief overview is provided here. Figure 1 shows a schematic of the system. The excitation laser system is a fibre-coupled type I optical parametric oscillator pumped by the 355 nm frequency tripled output of a *Q*-switched Nd:YAG laser. This provides 8 ns optical pulses over the wavelength range 410–2100 nm at a pulse repetition frequency (PRF) of 10 Hz. The output of the laser system is directed on to the sensor head, which is placed in acoustic contact with the skin.

The sensor head comprises a wedged PMMA substrate with a polymer film Fabry–Perot interferometer (FPI) formed on the lower side. The FPI is fabricated by vacuum depositing a

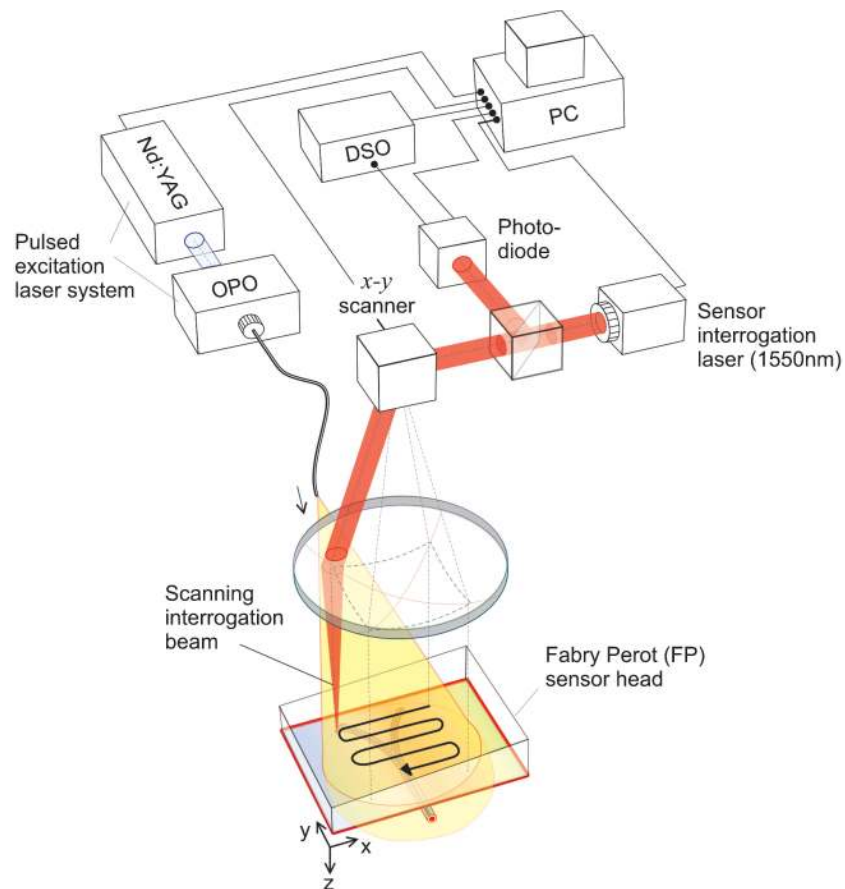


Figure 1. Photoacoustic imaging system. The Fabry–Perot (FP) sensor head is placed in acoustic contact with the surface of the skin. Nanosecond excitation laser pulses emitted by a tuneable OPO laser system are directed on to the sensor head, and transmitted through it into the underlying tissue thereby exciting acoustic waves. A second laser operating at 1550 nm provides a focused sensor interrogation laser beam that is raster scanned over the surface of the sensor to map the distribution of the photoacoustic waves arriving at the sensor head. From the 2D distribution of the photoacoustic waves, a 3D image is then reconstructed.

thin-film structure comprising a Parylene C polymer film spacer sandwiched between a pair of dichroic soft dielectric mirrors. These mirrors are highly reflective (>95%) between 1500 and 1650 nm but highly transmissive between 600 nm and 1200 nm. Thus, excitation laser pulses in the latter wavelength range can be transmitted through the sensor head and into the underlying tissue. Absorption of the laser energy produces photoacoustic pulses which propagate back to the sensor head where they modulate the optical thickness of the FPI and hence its reflectivity. The sensor is then read-out by raster scanning a focussed interrogation laser beam at 1550 nm (where the FPI mirrors are highly reflective) over the surface of the sensor using a galvanometer based x – y scanner. At each point of the scan, the sensor is optimally biased by tuning the interrogation laser wavelength to the point of maximum slope on the interferometer transfer function (ITF), the relationship between reflected optical power and phase. It is necessary to perform this biasing procedure at each point of the scan because the optical thickness of the polymer film spacer, and therefore the optimum bias wavelength, varies from point to

point. Under these conditions, the transduction mechanism can be regarded as one in which an acoustically induced modulation of the optical thickness of the FPI produces a small phase shift which is linearly converted, via the ITF, to a corresponding reflected optical power modulation. This time-varying optical power modulation, which represents the photoacoustic waveform, is detected by an ac-coupled InGaAs photodiode-transimpedance amplifier unit and recorded using a digital storage oscilloscope (DSO).

Once a waveform has been acquired at a particular spatial point on the sensor, it is stored within the onboard memory of the DSO. The interrogation laser beam is then moved to the next scan point and the procedure repeated. At the end of the 2D scan the entire set of waveforms are downloaded from the DSO to the PC and input to a k-space backpropagation algorithm (Koestli *et al* 2001) in order to reconstruct a 3D image of the initial pressure distribution: the photoacoustic image. The entire system is fully automated with the excitation and interrogation lasers, the optical scanner and DSO all under the control of a PC.

2.2. System performance

The maximum area over which the interrogation laser beam can be scanned is defined by a circle of diameter 50 mm. The $1/e^2$ diameter of the laser beam at its focus is $64\ \mu\text{m}$ and this represents, to a first approximation, the acoustically sensitive area (Cox and Beard 2007). The minimum step size is $10\ \mu\text{m}$ and is limited by the 12-bit resolution of the PC digital-to-analogue conversion card that controls the optical scanner. The acquisition speed of the system described in Zhang *et al* (2008) was approximately 1 s per scan step. This was limited by the sequential nature of the waveform downloading process in which each photoacoustic waveform was downloaded to the PC via a GPIB interface immediately following its acquisition. In this study, a different acquisition approach was adopted whereby the complete set of waveforms acquired over the scan were stored within the on-board memory of the DSO and downloaded to the PC in a single step. Although this enabled the point-to-point acquisition time of the scanner itself to be reduced to 10 ms, the average acquisition time achieved in this study was limited by the 10 Hz PRF of the OPO laser system to 100 ms per scan step.

Two different sensors were used in this study. One employed a $38\ \mu\text{m}$ thick FPI polymer spacer and provided a $-3\ \text{dB}$ acoustic bandwidth of 22 MHz. The other had a $22\ \mu\text{m}$ thick spacer and provided a $-3\ \text{dB}$ bandwidth of 39 MHz. In both cases, the frequency response is characterized by a smooth roll-off to zero. The frequency at which this zero response occurs is 58 MHz for the $38\ \mu\text{m}$ sensor and 100 MHz for the $22\ \mu\text{m}$ sensor. The low-frequency response is defined by the 100 kHz $-3\ \text{dB}$ cut-off frequency of the ac-coupled photodiode. The peak noise-equivalent pressure (over a measurement bandwidth of 20 MHz) of the $38\ \mu\text{m}$ sensor is approximately 0.2 kPa and 0.3 kPa for the $22\ \mu\text{m}$ sensor. These NEP figures are broadly comparable to the NEP of a 1 mm diameter PVDF piezoelectric receiver.

The instrument line spread function (LSF) represents a measure of the spatial resolution that the system can provide and is discussed in detail in Zhang *et al* (2008). The lateral LSF depends upon a variety of factors, among them the overall detection aperture (the scan area), the effective element size, spatial sampling interval and the bandwidth of the sensor. Furthermore, it depends on the angular aperture subtended by the detection aperture and therefore the axial and lateral position of the source. For these reasons, it is difficult to provide a single figure for the lateral LSF. However, taking into account the scan areas (between $1\ \text{cm}^2$ and $4\ \text{cm}^2$) used in the current study, the experimental data presented in Zhang *et al* (2008) suggest a lateral LSF in the range $50\ \mu\text{m}$ – $100\ \mu\text{m}$ for depths up to 5.5 mm at the centre of the detection aperture for both sensors. Unlike the lateral LSF, the vertical LSF is, to a first approximation, spatially invariant and dependent largely on the sensor bandwidth, which is

defined by the thickness of the polymer film spacer. Again, using the measurements obtained in Zhang *et al* (2008), the vertical LSF is estimated to be approximately 30 μm for the 38 μm sensor and 20 μm for the 22 μm sensor.

3. Results

To demonstrate the utility of the system for visualizing superficial blood vessels, images of the vasculature in the skin, and in tumours implanted in mice, were obtained. All images were obtained non-invasively, without signal averaging and using an incident fluence below the safe maximum permissible exposure (MPE) for skin (British Standard 1994). To aid the visualization of deeply lying features, a depth-dependent scaling factor was applied to the reconstructed images to compensate for optical attenuation. Apart from this and the use of an interpolation algorithm, no other image processing was employed. The reconstructed images in this paper are presented as maximum intensity projections or volume-rendered representations. The latter are also available as animated volume-rendered images and can be viewed as movie files online (or downloaded) at stacks.iop.org/PMB/54/1035 or the University College London website³. These animations provide the most compelling demonstrations of the 3D imaging capability of the system.

3.1. Human palm

An *in vivo* image of the subcutaneous vasculature in the palm of a volunteer was obtained using the 38 μm FP sensor. The sensor head was placed over the region of interest on the palm with a gap of few hundred microns between the surface of the skin and the sensor. A drop of water was inserted in the gap in order to provide the necessary acoustic coupling. The OPO was set to an excitation wavelength of 670 nm. The laser fluence incident on the skin surface was 10 mJ cm^{-2} and thus below the MPE of 20 mJ cm^{-2} for skin at this wavelength (British Standard 1994). The photoacoustic signals were mapped by scanning the sensor interrogation beam over an area of 20 mm \times 20 mm in steps of 250 μm and acquiring a photoacoustic waveform at each step with a single laser pulse. The total number of waveforms acquired was therefore 6400 and the time taken to acquire them was approximately 10 min. A 3D image of dimensions 20 mm \times 20 mm \times 6 mm was then reconstructed from the detected signals using the 3D k-space backpropagation algorithm referred to in section 2.1.

Figure 2 shows a volume-rendered representation of the reconstructed image and a series of lateral slices at different depths. These images show the subcutaneous vasculature to a depth of approximately 4 mm—the deepest lying vessel is indicated by the arrow 'A' on both the volume-rendered image and the deepest lateral slice. Figure 3(a) shows a lateral maximum intensity projection (MIP). This was obtained from the 3D reconstructed data set by projecting the maximum value of voxels lying along the z -direction on to the x - y plane. Figure 3(b) shows a single vertical slice through the centre of the lateral MIP as indicated. This vertical slice further illustrates the depth-resolved nature of the technique with the contour of the skin surface as well as several underlying sub-dermal blood vessels visible.

3.2. Mouse skin

An *ex vivo* image was obtained of the microvasculature in the skin around the abdomen of a 3 month old mouse (CL57/BL6) using the 38 μm FP sensor. The animal was prepared by removing the hair around the region of interest using hair removal cream. As in the study

³ <http://www.medphys.ucl.ac.uk/research/mle/images.htm>

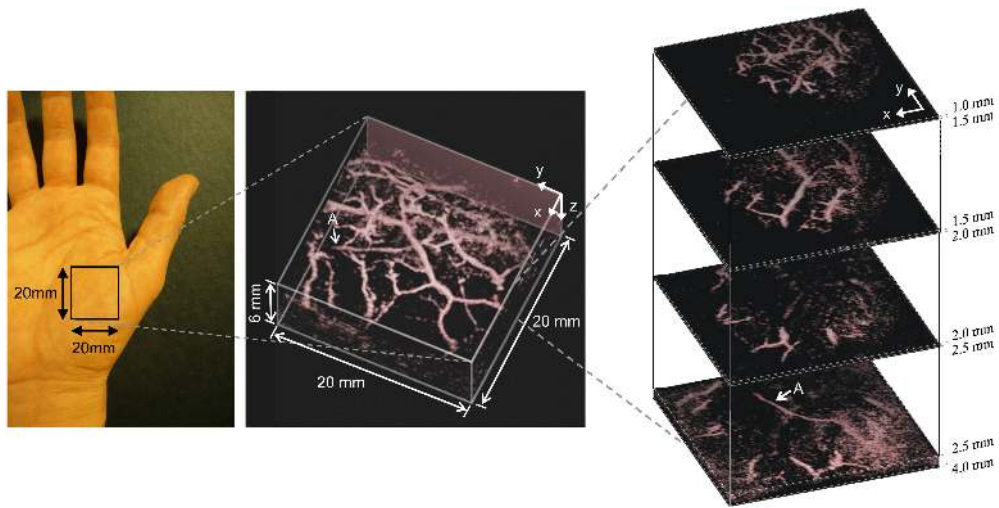


Figure 2. *In vivo* photoacoustic image of the vasculature in the palm using an excitation wavelength of 670 nm. Left: photograph of the imaged region, middle: volume rendered image. An animated representation of this image can be viewed at stacks.iop.org/PMB/54/1035, and right: lateral slices at different depths. The arrow 'A' indicates the deepest visible vessel, which is located 4 mm beneath the surface of the skin.

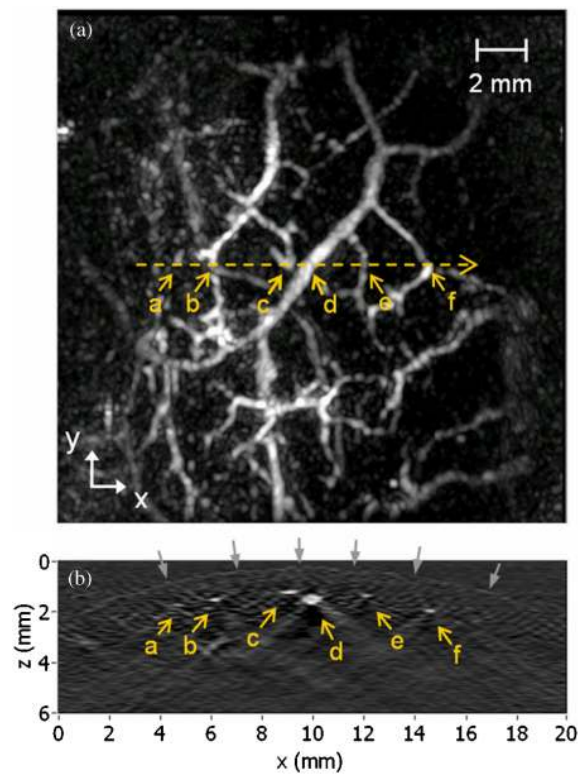


Figure 3. (a) Lateral maximum intensity projection (MIP) of the 3D image of the human palm shown in figure 2. (b) Vertical slice image along yellow dotted lines shown in lateral MIP. Grey arrows indicate the contour of the skin surface.

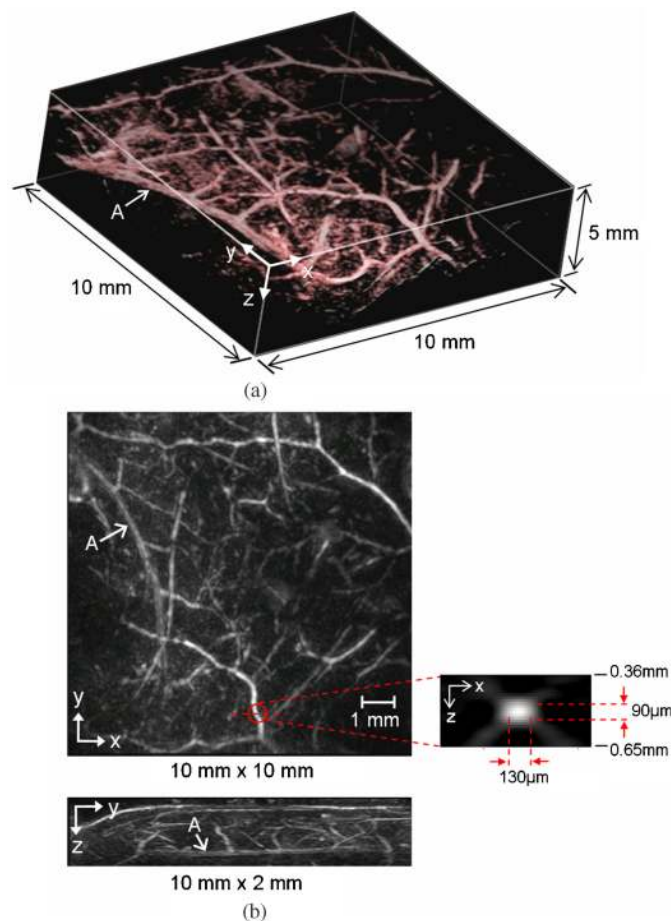


Figure 4. Photoacoustic image of the vasculature in the skin around the abdomen of the mouse obtained using an excitation wavelength of 590 nm. (a) Volume rendered image. An animated representation of this image can be viewed at stacks.iop.org/PMB/54/1035 (b) Top: lateral maximum intensity projection (MIP). Image on the right is a vertical slice in the x - z plane showing a cross-sectional view of the blood vessel indicated. The dimensions shown are full width half-maximum values. Bottom: vertical MIP. The arrow 'A' indicates the deepest visible vessel, which is located 2 mm beneath the skin surface.

described in the previous section, the skin was acoustically coupled to the sensor head with a drop of water although on this occasion the skin was placed in direct contact with the sensor head. The OPO output was set to a wavelength of 590 nm, the incident fluence was 6.8 mJ cm^{-2} and the photoacoustic signals were mapped over an area of $10 \text{ mm} \times 10 \text{ mm}$ in steps of $100 \mu\text{m}$. The total time taken to acquire all 10 000 signals was approximately 16 min. The reconstructed image is shown as a volume-rendered representation in figure 4. The higher optical attenuation by blood at 590 nm compared to 670 nm resulted in a lower penetration depth than obtained in section 3.1. As a consequence, the deepest observable vessel is located at a depth of 2 mm. Figure 4(b) shows the corresponding lateral and vertical MIPs. Compared to the image of the human palm in which the vessel diameters are of the order of a few hundred microns, significantly smaller vessels can be seen. This is a consequence of the increased spatial resolution achieved due to the smaller scan step size of $100 \mu\text{m}$, and is most apparent

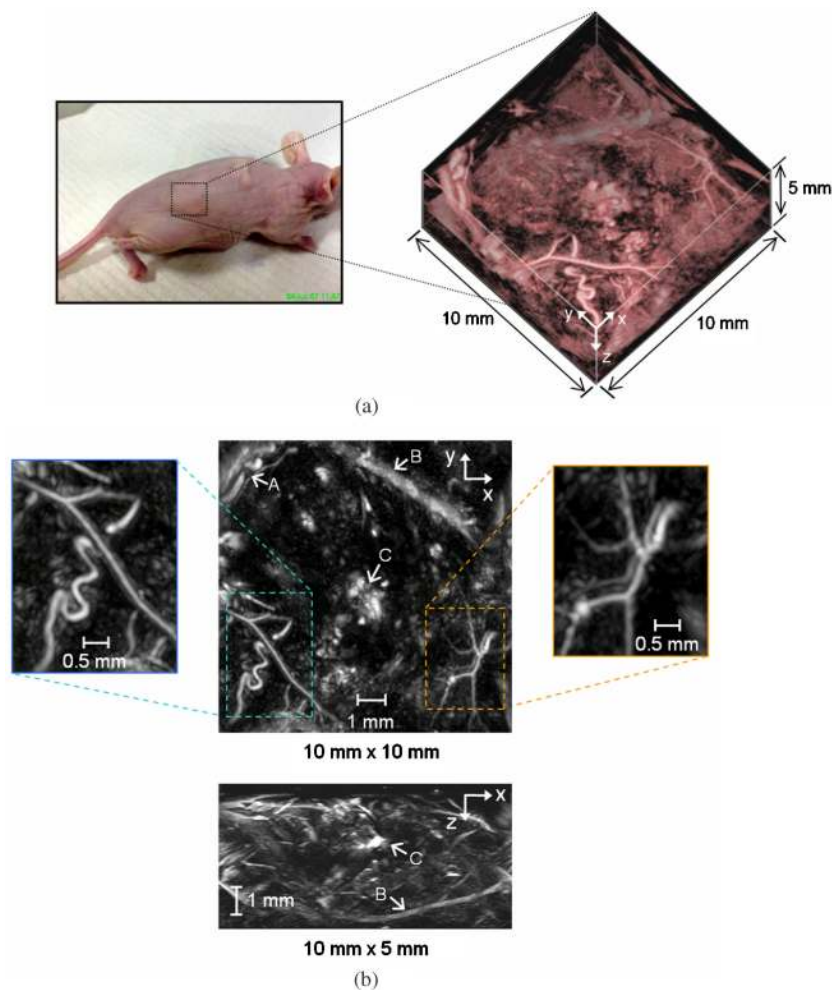


Figure 5. Photoacoustic image of LS174T tumour obtained using an excitation wavelength of 650 nm. (a) Volume rendered image. An animated representation of this image can be viewed at stacks.iop.org/PMB/54/1035, (b) Top: lateral (x - y) maximum intensity projection (MIP), *left and right*: expanded views, bottom: vertical (x - z) MIP. The expanded views and the vessels marked 'A' and 'B' show peripheral supplying tumour vessels. The region marked 'C' shows a region consistent with a local increase in microvascular density.

in the vertical cross-sectional image through the vessel shown in figure 4(b). The lateral and vertical FWHM dimensions of the reconstructed feature are $130 \mu\text{m}$ and $90 \mu\text{m}$, respectively. The larger lateral dimension is consistent with the higher vertical resolution that a planar detection geometry provides due to its finite detection aperture.

3.3. Implanted tumours

Mouse models are used to study the pathophysiology of a wide variety of tumours to aid the development and refinement of new cancer therapies. A common approach is to implant a subcutaneous tumour and study its progression over time. Characterizing the structure of the tumour vasculature is important as it can affect the development of the tumour and its

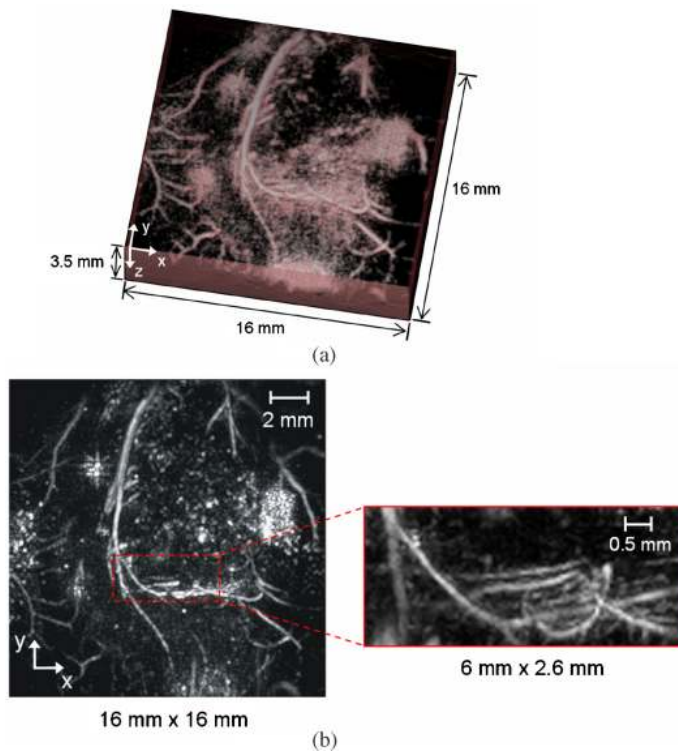


Figure 6. Photoacoustic image of SW1222 tumour obtained using an excitation wavelength of 650 nm. (a) Volume-rendered representation, (b) Left: lateral (x - y) maximum intensity projection (MIP) (An animated representation of this image can be viewed at stacks.iop.org/PMB/54/1035). Right: expanded view obtained by rescanning the area indicated with a smaller scan step.

response to treatment. To demonstrate the utility of the instrument for this purpose, two human colorectal tumour models were imaged. The first of these, the human colorectal adenocarcinoma xenograft LS174T, was grown to a size of approximately $8\text{ mm} \times 8\text{ mm}$ in the flank of a female nude MF1 mouse as indicated in the photograph in figure 5(a). The OPO was set to a wavelength of 650 nm and the photoacoustic signals were mapped over an area of $10\text{ mm} \times 10\text{ mm}$ in steps of $100\text{ }\mu\text{m}$ using the $22\text{ }\mu\text{m}$ sensor. The reconstructed image is shown as a volume-rendered representation in figure 5(a) and lateral and vertical MIPs in figure 5(b). The animated volume-rendered representation available online (stacks.iop.org/PMB/54/1035) shows the 3D structure of the vasculature to best effect. The images in figure 5 reveal a poorly and heterogeneously vascularized core supplied by networks of larger vessels around its periphery: examples of these larger supplying vessels are those labelled ‘A’ and ‘B’, and the vessels in the expanded views of the lateral MIP. Within this peripheral vascular network lie discrete patches of contrast (for example the region marked ‘C’) that may indicate a local increase in the density of capillaries and other microvessels—these regions do not resemble recognisable vascular structures as the system is not able to resolve individual capillaries. These features are broadly consistent with the heterogeneity and low microvascular density that this type of tumour is known to exhibit (El-Emir *et al* 2007). Feature characteristics of tumour vessels in general, such as tortuous paths and abnormal branching patterns, can also be seen, most obviously in the expanded MIPs in figure 5(b). Note also that the vertical MIP

shows that the tumour was imaged to a depth of approximately 5 mm as evidenced by the large vessel (labelled 'B'), which traverses the underside of the tumour.

A second human colorectal tumour model with a different pathophysiology, the SW1222, was also imaged. This tumour was grown in the flank of a nude mouse as in the previous case but to a larger size of approximately 20 mm × 20 mm. The excitation wavelength was 630 nm and the photoacoustic signals were mapped over an area of 16 mm × 16 mm in steps of 100 μm using the 22 μm sensor. This tumour is characterized by a more homogeneous vascular architecture and higher microvascular density than the LS174T tumour (El-Emir *et al* 2007). This can be seen in the volume-rendered image in figure 6(a), which shows patches of relatively uniform contrast along with a number of larger supplying tumour vessels. The latter are distributed around the body of the tumour with their peripheral nature being most apparent in the animated volume rendered image that is available online (stacks.iop.org/PMB/54/1035). The expanded view of the lateral MIP in figure 6(b), obtained by rescanning a 6 mm × 2.6 mm region of the tumour with a finer sampling interval of 60 μm, shows a further example of the chaotic and tortuous nature of tumour vessels.

4. Conclusions

The use of a novel photoacoustic imaging instrument for visualizing the vasculature in 3D to depths of up to 5 mm with sub-100 μm spatial resolution has been demonstrated. There are several advantages of the system over other photoacoustic imaging instruments used for imaging blood vessels to mm depths. The transparent nature of the sensor avoids the difficulties posed by the opaque nature of piezoelectric receivers in delivering the excitation laser light to the skin surface, allowing a truly backward mode detection configuration to be achieved. In addition, the sensor provides a level of acoustic performance that can be difficult to achieve with piezoelectric-based detection methods, particularly in relation to the spatial sampling of the incident acoustic field. Because the sensor is optically addressed using a focused laser beam, the incident acoustic field can be spatially sampled with significantly higher (potentially optical diffraction limited) resolution than can be achieved with piezoelectric receivers. It is this along with the broadband uniform acoustic frequency response of the sensor and its high detection sensitivity that are responsible for the high contrast and spatial fidelity of the reconstructed images. As noted in Zhang *et al* (2008) there is also significant potential to further improve the imaging performance in terms of penetration depth and increasing the sensor bandwidth and optimizing the spatial sampling parameters to obtain higher spatial resolution. There is also scope to increase acquisition speed, potentially obtaining real time image acquisition rates, through the increasing availability of higher repetition rate laser systems (Allen and Beard 2006, Maslov *et al* 2007), or parallelizing the sensor read-out scheme using a photodetector array as described in Lamont and Beard (2006).

In summary, it is considered that this system may find a role for high-resolution soft tissue imaging applications. These could include characterizing the structure and function of superficial vascular networks for the assessment of skin tumours, vascular lesions, soft tissue damage such as burns and wounds and other superficial tissue abnormalities characterized by changes in tissue perfusion. In addition, it could be used, as indicated in this study, for characterizing tumour vasculature in small animal models.

References

- Allen T J and Beard P C 2006 Pulsed NIR laser diode excitation system for biomedical photoacoustic imaging *Opt. Lett.* **31** 3462–64

- Beard P C 2001 Flow velocity measurements UK Patent Application WO 03/039364
- British Standard 1994 BS EN60825-1
- Cox B T and Beard P C 2007 Frequency dependent directivity of a planar Fabry Perot polymer film ultrasound sensor *IEEE Trans. Ultrason. Ferroelectr. Freq. Control* **54** 394–404
- El-Emir E, Qureshi U, Dearling J L J, Boxer G M, Clatworthy I, Folarin A A, Robson M P, Konerding M A, Nagl S and Pedley R B 2007 Predicting response to radioimmunotherapy from the tumor microenvironment of colorectal carcinomas *Cancer. Res.* **67** 11896–905
- Fang H, Maslov K and Wang L V 2007 Photoacoustic Doppler effect from flowing small light-absorbing particles *Phys. Rev. Lett.* **99** 184501
- Koestli K, Frenz M, Bebie H and Weber H 2001 Temporal backward projection of optoacoustic pressure transients using Fourier transform methods *Phys. Med. Biol.* **46** 1863–72
- Lamont M and Beard P C 2006 2D imaging of ultrasound fields using a CCD array to detect the output of a Fabry Perot polymer film sensor *Electron. Lett.* **42** 187–9
- Lao Y, Zhou F and Wang H 2008 *In vivo* photoacoustic imaging of subcutaneous vasculature and vascular anomalies in small animals *Eur. Phys. J. Appl. Phys.* **41** 151–5
- Laufer J G, Delpy D T, Elwell C E and Beard P C 2007 Quantitative spatially resolved measurement of tissue chromophore concentrations using photoacoustic spectroscopy: application to the measurement of blood oxygenation and haemoglobin concentration *Phys. Med. Biol.* **52** 141–68
- Maslov K, Zhang H F and Wang L V 2007 Portable real-time photoacoustic microscopy *Proc. SPIE* **6437** 643727–1
- Niederhauser J J, Jaeger M, Hejazi M, Keppner H and Frenz M 2005 Transparent ITO coated PVDF transducer for optoacoustic depth profiling *Opt. Commun.* **253** 401–6
- Oh J T, Li M L, Zhang H F, Maslov K, Stoica G and Wang L V 2006 Three-dimensional imaging of skin melanoma *in vivo* by dual-wavelength photoacoustic microscopy *J. Biomed. Opt.* **11** 034032-1–034032-4
- Siphanto R I, Kolkman R G M, Huisjes A, Pilatou M C, de Mul F F M, Steenbergen W and van Adrichem L N A 2004 Imaging of small vessels using photoacoustics: an *in vivo* study *Lasers Surg. Med.* **35** 354–62
- Viator J A, Au G, Paltauf G, Jacques S L, Prahl S A, Ren H, Chen Z and Nelson J S 2002 Clinical testing of a photoacoustic probe for port wine stain depth determination *Lasers Surg. Med.* **30** 141–8
- Xu M and Wang L V 2006 Photoacoustic imaging in biomedicine *Rev. Sci. Instrum.* **77** 041101
- Wang L V 2008 Tutorial on photoacoustic microscopy and computed tomography *IEEE J. Sel. Top. Quantum Electron.* **14** 171–9
- Zhang E Z, Laufer J and Beard P C 2007 Three dimensional photoacoustic imaging of vascular anatomy in small animals using an optical detection system *Proc. SPIE* **6437** 643710S-1–8
- Zhang E, Laufer J and Beard P C 2008 Backward-mode multiwavelength photoacoustic scanner using a planar Fabry Perot polymer film ultrasound sensor for high resolution three-dimensional imaging of biological tissues *Appl. Opt.* **47** 561–77
- Zhang H F, Maslov K, Li M, Stoica G and Wang L V 2006a *In vivo* volumetric imaging of subcutaneous microvasculature by photoacoustic microscopy *Opt. Express* **14** 9317–23
- Zhang H F, Maslov K, Stoica G and Wang L V 2006b Functional photoacoustic microscopy for high-resolution and noninvasive *in vivo* imaging *Nat. Biotechnol.* **24** 848–50
- Zhang H F, Maslov K M, Soica G and Wang L V 2006c Imaging acute thermal burns by photoacoustic microscopy *J. Biomed. Opt.* **11** 054033-1